A Variable Sky-View Platform for the Measurement of Ultraviolet Radiation

CHRISTOPHER KUCHINKE AND MANUEL NUNEZ

School of Geography and Environmental Studies, University of Tasmania, Sandy Bay, Tasmania, Australia

ABSTRACT

One of the more difficult tasks confronting atmospheric researchers today is the acquisition of long-term radiometric measurements that encapsulate variability in the sky hemisphere as well as time. High quality spatial measurements would allow for a greater understanding of atmospheric processes, both specific to the site and between locations. This information would lead to further development of better spatial models for predicting future trends.

This study develops a timer-controlled variable sky-view platform (VSP), designed to encapsulate both the spatial and temporal variation of radiation in the sky hemisphere for Hobart, Australia (42.90°S, 147.33°E). The VSP essentially allows for a sensor to move up and down inside a fixed cylinder, therefore causing the sky-view factor to vary. A full description of the VSP design, electronics, and construction is given. Emphasis is on high-precision long-term operation under all weather conditions. A modeling scheme and output results illustrate the advantages of the VSP over current sky-observing instruments. It can accurately parameterize the direct and diffuse erythemal irradiance as well as the azimuthally integrated erythemal sky radiance distribution for every 2-min duration (at the current setting). In addition, all data can be obtained for clear-sky and cloudy conditions.

The VSP is currently in use with the erythemal ultraviolet (UV) biometer 501-A manufactured by Solar Light Company, Inc. (SLC). As such, it provides an additional source of UV sky distribution data to the Hobart UV-climatology database.

1. Introduction

Many measurement campaigns have been previously undertaken in an attempt to harness the spatial component of the radiance field for a given location. Literature pertaining to measurements of sky radiance under clear skies all show that the radiance distribution across the sky is anisotropic (e.g., Beaglehole and Carter 1992; Blumthaler et al. 1996; Grant et al. 1997a and others). Similarly, cloudy-sky radiance distribution measurements have been undertaken for different cloud scenarios (e.g., Weihs et al. 2000).

In most studies, sky radiance measurements attempt to encapsulate the entire sky hemisphere in terms of both zenith and azimuthal components. However, measurements are time intensive, and, as a consequence, any representative scan of the whole sky is composed of samples that are not instantaneous with respect to each other. For example, the sky-tracking and measurement times presented in many papers can vary significantly, from 8 min (Blumthaler et al. 1996) through 15 min (Weihs et al. 2000) to as high as 30 min (Grant et

al. 1997a) and beyond. It is obvious that during this period, the sky radiance distribution may change significantly. This will affect model results designed to replicate the UV sky radiance distribution.

Generally speaking, three factors contribute to the amount of time required for a complete, representative scan: the angular resolution of the measurements, the response time of the sensor facility, and the tracking movement of the system. An attempt to reduce the angular resolution of the measurements results in the need for extra interpolation between angles. This in turn leads to additional error. However, advancements in technology have lead to vast improvements in the speed of the monochromator assembly and tracking movement of spectral instruments, enabling higher-resolution sky scans. For example, new breeds of monochromators focus light from the monochromator grating onto a series of diode arrays. Although array instruments still contain stray light problems, their fast sampling is a step toward measurement of the complete sky field in representative time, as evidenced by the work of Nield et al. (1997) for a Hamamatsu 512-element silicon diode array.

This study presents the variable sky-view platform (VSP)—a new methodology for fast retrieval of sky radiance distribution information at relatively low setup cost. The system is intended for use with any π field-of-view sensor. Essentially, the deployed instrument

Corresponding author address: Dr. Christopher Kuchinke, School of Geography and Environmental Studies, University of Tasmania, GPO Box 252-78, Sandy Bay, Tasmania 7001, Australia.
E-mail: kuchinke@utas.edu.au

moves up and down within a shading cylinder, therefore varying the amount of sky that the sensor receives. The design is thus implemented in order to dispense with a sophisticated tracking device.

The sensor selected for VSP deployment is the Solar Light Company, Inc. (SLC), UV biometer 501-A. This broadband instrument is regularly employed for the estimation of UV-B because of its high resilience and low cost. Since its inception from the original Robertson–Berger meter (Robertson 1972), temperature correction and improved filter construction has led to a more precise instrument (Morys and Berger 1993). In addition, the filter in the instrument approximates the erythemal flux, adding impetus to its inclusion in the VSP.

2. Methodology

The measurement platform site utilized in this study rests 38 m above mean sea level. It is located on the roof of the Geography building at the University of Tasmania, Sandy Bay campus (42.90°S, 147.33°E), situated 3 km south of the Hobart city center. The site consists of a large instrument mounting bench and facilities for dry equipment storage, power supply, and computer network connection. The platform floor is covered by bituminous sheeting and has a UV albedo of 0.08.

a. The variable sky-view platform

The SLC instrument moves up and down within an inflexible vertically aligned polyvinyl chloride (PVC) cylinder. Movement is performed by a hydraulic system driven by an electric motor. At any point in time, the fixed cylinder will shade the sensor by a known portion of the sky. In this section and for the remainder of the study, the zenith sky view (ZSV) is defined as half the VSP sky-view angle and is only applicable to measurements of irradiance. In turn, the sky-view angle is defined as twice the angle subtended by the vertical to the sensor and a line from the sensor to the top edge of the cylinder (Fig. 1).

With reference to the moving sensor, we shall hereafter refer to a complete downward movement from top to bottom (or vice versa) as one run. For any upward run, we can isolate the direct beam by taking the global irradiance difference between when the sensor last senses no sun to when it first senses a full sun (shown by instrument filter positions A and B in Fig. 1). The opposite applies to a downward run. The diffuse irradiance is subsequently calculated by subtracting this direct beam from the global irradiance measurement at the top of the same run. From any single run, the sky can be partitioned into discrete intervals of ZSV. A schematic of the overall VSP system is given in Fig. 2, and a brief description of components is as follows.

A vertical stainless-steel hydraulic shaft is free to move within the fixed cylinder, controlled by indepen-
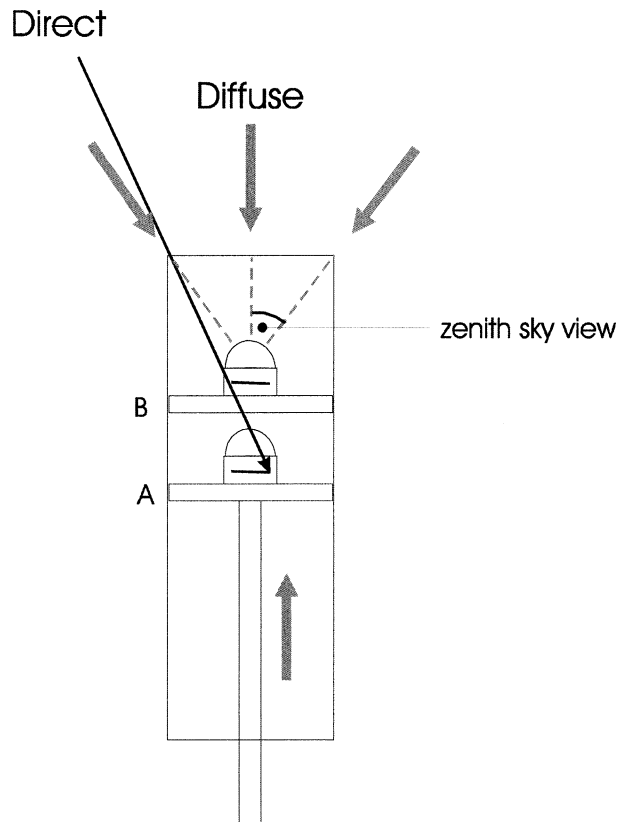

FIG. 1. Basic geometry of the VSP: A = no-sun view, B = full-sun view.

dent "up" and "down" variable-speed valves. The valves can be adjusted to allow for a range in shaft movement of between 0.3 and 5 cm s^{-1}. A 0.55-kW electric motor drives the system in conjunction with an oil reservoir. Laboratory timing tests conducted over many hours indicated that upon valve speed selection, the movement of the shaft is constant. To allow for a custom fit of the SLC instrument within the shading cylinder, its cable-connection socket was first shortened and a hole was drilled through the housing base support of the SLC instrument, directly beneath the cable exit port. The instrument cable was then passed down through the hole to a movable pulley at the bottom of the guide pipe, then back up to the top of the support frame where it was fixed (Fig. 2). The pulley itself is weighted, and the complete setup ensures that the SLC cable remains tangle free during movement. A galvanized steel frame (1.5-m height, 1-m square) provides the main support framework for the VSP and is securely bolted at all corners to the station floor. The VSP shading cylinder rests in its own housing, which is bolted to the main support frame. Tension cables connect the top of the cylinder to the four upper corners of the main support frame. This ensures that the cylinder does not move during periods of high wind speed. Everything is adjusted for level and plumb.
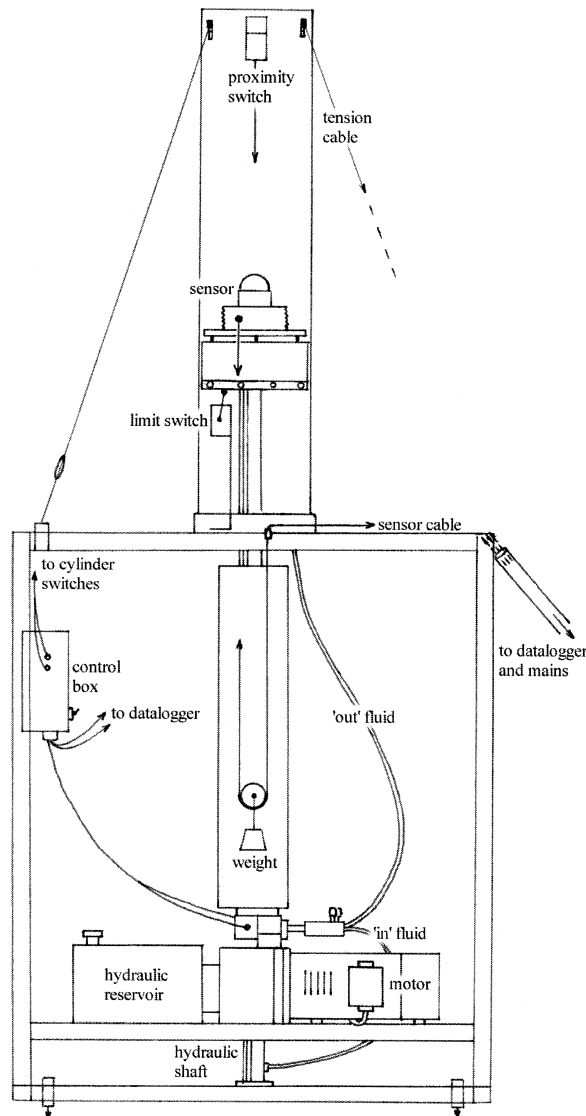
FIG. 2. Crude schematic of the VSP.

VSP power control is via a mains timer switch placed in series between a side-mounted waterproof switchboard and mains power supply. This allows for the hydraulics to be automatically activated and shut down at sunrise and sunset, respectively. Hydraulic status of the VSP (up, down, or stationary) is provided by a bottom "limit" and top "proximity" switch with respect to the cylinder. Activation of either switch by instrument movement triggers an electrical signal at the switchboard, resulting in reversal of the hydraulics. The switchboard also contains a time-delay relay. This is activated for about 5 s when the sensor is at the top of the cylinder and allows for a stable global measurement during this time.

A Cambell Scientific, Inc., CR10 datalogger continuously receives the VSP hydraulic status and outputs a result-dependent flag. It also receives the signal output

from the VSP sensor and a similar SLC UV biometer situated 5 m from the VSP. Both instruments sample every 0.75 s. This sampling limit is directly related to the time constant of the SLC instrument, determined experimentally as 0.141 s (equating to just under 0.75 s to reach 99.5% of a step change value). Furthermore, a nearby pyranometer activates the datalogger if its signal output is greater than 10 W m^{-2}. This ensures that the datalogger is idle for all SZAs greater than approximately 85°.

Finally, an 18-bit counter achieves a positional fix of the VSP-deployed sensor. Accuracy is governed by a 2-MHz oscillating crystal. The counter increments linearly until either the bottom limit or top proximity switch is activated, then it is reset to zero. Each time the datalogger records the instrument signal it simultaneously provides the signal for "latching" and reading of the count. Thus, to calculate the corresponding VSP height of any output signal, any recorded latch count is downscaled to the cylinder height as follows:

partial height

$$= \frac{\text{recorded latch count} \times \text{total height}}{\text{total latch count}}, \quad (1)$$

where the total latch count for a particular run is calculated using the last count from the current run, the first count from the following run, and the knowledge that the counter increments equally between samples. Knowledge of the partial height allows for the determination of the instrument sky-view factor for any point in time.

b. VSP optics

A flat-black paint was applied to the inside of the PVC cylinder to minimize UV reflection. In order to increase the Lambertian properties of the surface, some small perspex particles (50–100-μ diameter) were mixed with the paint at 300 g L^{-1}. A Macam Photometrics, Ltd., SR9910 spectroradiometer was then used to quantify the (spectrally averaged) UV Lambertian and albedo properties of the surface, with the latter determined to be 0.0185. Both parameters were then incorporated into a Monte Carlo model designed to encapsulate the cylinder internal reflection for the entire scheme. After application of this model it was found that the internal reflection of UV light within the cylinder was negligible.

The height and speed settings of the VSP also affect the optical performance of the system. Given that the speed of the VSP hydraulics is always constant, the relative ZSV resolution of the sensor is decreased as it moves upward within the cylinder. One way to address this problem is to vary the duration of each run. However, this presents a limiting factor. The run time must not be too long, or else the VSP data lose integrity due to the possible change in the sky radiation field over
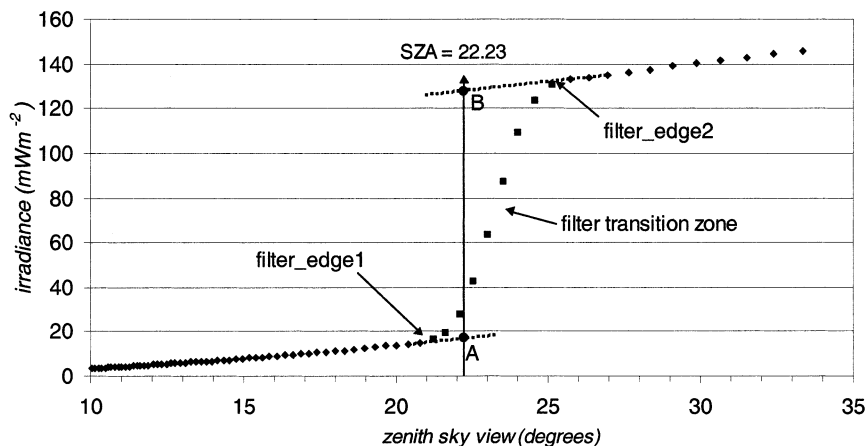
FIG. 3. Example of raw UV-B measurements from a single VSP run, 17 Jan 2000: start time = 1233:32.75 EST, SZA = 22.23°, VSP height = 729.5 mm.

this time. An alternate method to improve the ZSV resolution of the VSP is to alter the total distance that the cylinder travels within the cylinder. Although various heights have been used in the scheme, the optimum VSP height setting was determined to be 459.0 mm. This gives an excellent sky-view resolution for an instrument near the top of the cylinder. It also provides for adequate sensor sensitivity at low to moderate SZAs for an instrument at the bottom, where the ZSV approximates 10°.

Of final mention here is the relationship between the SLC phosphor filter and the sky-view factor of the VSP. The 3.0-mm-thick black glass optical filter is clearly situated under the UV-transmitting quartz weather dome. It cuts off most of the visible and infrared portions of the spectrum but does not act as a diffuser (Dichter 1993). The UV-diffusing plane of the SLC instrument (and hence VSP sky-view focal plane) is in fact the top of the phosphor filter diffuser plate. This is situated 1.22 mm below the bottom-surface of the black glass, which is true for all SLC detectors with serial numbers above 1000 (W. Eckman 2000, personal communication). Error as a result of blockage by the instrument housing itself is deemed to be accounted for during instrument cosine response correction (Kuchinke and Nunez 2001). Additionally, the radius of the SLC phosphor filter is 7.95 mm. The outer perimeter of the filter is not used for VSP sky-view determination. The correct sky-view of the phosphor filter is determined from the effective radius (r_{eff}) at which the total response of the filter, as a function of area, is at a maximum. Analysis of a direct beam passed across the filter indicated a linear radial response, decreasing outward from the center of the filter. Subsequent incorporation of filter area into the analysis produced an r_{eff} value of exactly 2.80 mm. Hence, a diameter of 5.6 mm represented the correct filter perimeter for determination of the VSP sky view of the sensor.

c. VSP data processing

1) RETRIEVAL AND MODIFICATION OF DIRECT DATA

As just described, the sensor plane of the SLC is composed of a finite horizontal width. Thus, for an upward-moving sensor, a "dark" zone exists from the time (height) at which the filter edge first senses the corona of the sun (viz., filter_edge1) to when the opposite filter edge finally strikes the opposite side of the corona (viz., filter_edge2). This is because the whole filter must be exposed to a full sun for an accurate inclusion of the direct beam into the sensor signal.

Given this phenomenon, we shall call this time (or height) interval the "transition zone," defined hereafter as the zone whose geometric boundaries are determined by alignment of each given filter_edge with the top cylinder edge and the respective sun edge as described above. Similarly, we shall call the regions surrounding this zone the "before" and "after" zones from the bottom to the top of the cylinder, respectively. Figure 3 provides a detailed example of the cumulative signal output corresponding to one upward VSP run. Here, the square data points correspond to the measurements that lie in the described transition zone, and the SZA indicator line indicates the position of the center of the solar disk on the cumulative curve.

In order to determine the position of each filter_edge as shown in Fig. 3 for all VSP runs, two flags are first generated for every 0.75-s signal output from the instrument. The flags correspond to the ZSV of the opposite filter edges of the SLC instrument. They are calculated trigonometrically using the cylinder and filter radii and the height of the sensor in the cylinder. A subsequent comparison of the ZSV of each output flag with the SZA at the time of the measurement indicates whether each signal corresponds to a before, transition, or after zone. Allowance is made for the arc angle of the solar disk.

The VSP transition zone itself comprises the direct beam plus a relatively small portion of the total diffuse signal ΔD. It is impossible to exactly distinguish this circumsolar diffuse component very near to the sun from the direct beam with 100% certainty. Fortunately, the transition zone always corresponds to a relatively small change in ZSV. Hence, extrapolation of both before and after trend lines to the same abscissa point (A and B in Fig. 3) allows us to ascertain ΔD with a high degree of confidence.

On completion of these tasks it is rather straightforward to extract the direct beam for any VSP run. This is simply the difference between the upper and lower extrapolated values that intersect with the SZA indicator line as given in Fig. 3. A cosine correction as given by Kuchinke and Nunez (2001) is then applied to the extracted value to adjust the signal for instrument cosine response. Application of this correction requires the SZA at the time of the direct measurement, calculated as the average SZA for the corresponding 2-min run.

2) RETRIEVAL AND MODIFICATION OF DIFFUSE DATA

Retrieval of the diffuse component requires a straightforward subtraction of the direct beam from each observation in the after zone. This gives us a record of the cumulative diffuse irradiance for the entire run, with the total diffuse irradiance corresponding to the top-of-cylinder value. An important phenomena here is that each raw VSP signal changes according to the change in irradiance from the previous signal due to the addition or subtraction of sky view from the instrument field of view. The result is that the time-delay response of the instrument described earlier has an *opposite* effect on upward and downward VSP measurements. A time-constant correction algorithm was applied to each VSP signal to correct for this. The correction involved a "de-smoothing" iterative procedure contained in Panofsky and Brier (1968), and, for simplicity, it was assumed that the change in instrument response between consecutive signals was linear.

The cosine correction of the diffuse irradiance was undertaken as a stepwise procedure, again utilizing the direct-beam calibration curves of Kuchinke and Nunez (2001). Equation (2) and Fig. 4 illustrate the cosine correction algorithm. The raw irradiance at the bottom (R_1) is corrected for the cosine response of the instrument $C(\overline{\theta_1})$, where $\overline{\theta_1}$ for the initial value is defined as $(\theta_1 + \theta_2)/2$. This results in the corrected signal E_1. Successive corrections follow as shown in Eq. (2) for E_2 to E_n as the instrument traverses to the top:

$$E_1 = C(\overline{\theta_1})R_1 \qquad \theta_1 = (\theta_1 + \theta_2)/2$$

$$E_2 = E_1 + (R_2 - R_1)C(\overline{\theta_2}) \qquad \theta_2 = \theta_1 + (\theta_2 - \theta_1)/2$$

$$\vdots \qquad\qquad \vdots \qquad\qquad \vdots \qquad\qquad \vdots$$

$$E_n = E_{n-1} + (R_n - R_{n-1})C(\overline{\theta_n}) \qquad \theta_n = \theta_{n-1} + (\theta_n - \theta_{n-1})/2. \qquad (2)$$

The algorithm assumes that the signal changes linearly across each ZSV range. This is questionable for a sensor at the base of the shading cylinder due to the larger size of the "starting" arc angle. Fortunately, the cosine correction is very small for an instrument in this position. Therefore, the algorithm allows for accurate cosine correction of the whole cumulative diffuse curve, provided that the VSP sky-view resolution remains small.

3) RETRIEVAL AND MODIFICATION OF RADIANCE DATA

The relative movement of the shading-cylinder instrument arrangement allows for the sky to be partitioned into discrete intervals of sky view. In this study, we refer to this as the zenith discrete angle (ZDA), referenced to the 0° vertical as for ZSV. That is, both ZSV (for irradiance measurements) and ZDA (for radiance measurements) both imply a specific zenith angle. However, the ZDA represents a much small angular interval of sky centered at the given discrete angle (Fig. 5). Thus, to be exact, the VSP ZDAs refer to concentric ring portions of the sky sphere, azimuthally averaged and centered directly above the sensor.

To quantify this, the surface area (A) of the sky hemisphere as seen by the VSP sensor subtending a ZSV of θ can be given by

$$A = 2\pi r^2[1 - \cos(\theta_0)]. \qquad (3)$$

In terms of solid angle ($\Omega = A/r^2$), the above equation may be written as

$$\Omega = 2\pi(1 - \cos\theta_0) \quad \text{or} \qquad (4)$$

$$\delta\Omega = 2\pi \sin\theta_0 d\theta_0. \qquad (5)$$

From the previous expression, the measured irradiance in a finite ring can be given as

$$\overline{R}\cos\theta = \frac{\delta D}{\delta\Omega}, \qquad (6)$$

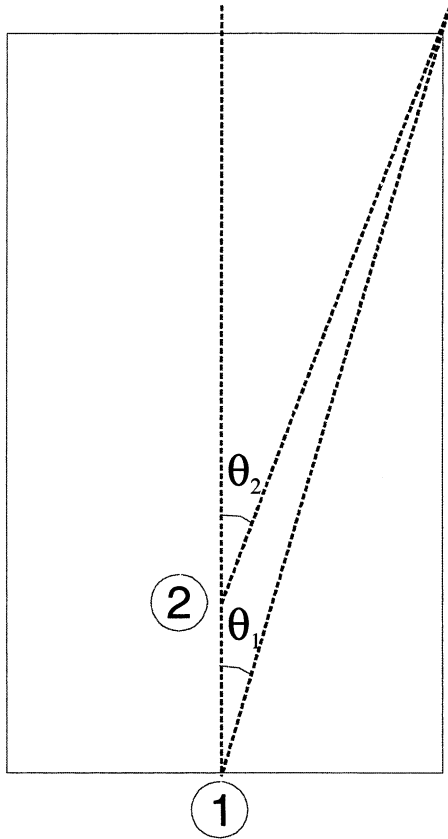where $\overline{R}$ is an azimuthally averaged radiance (in mW

FIG. 4. Diagram showing the geometry of the cosine correction algorithm: θ_1 and θ_2 are the lowest and second lowest ZSVs, corresponding to positions 1 and 2, respectively.
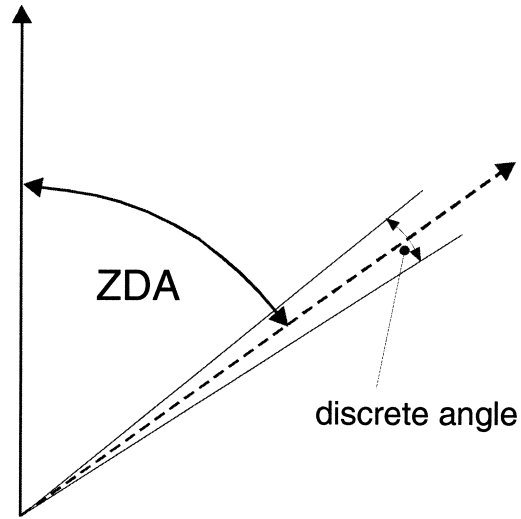

FIG. 5. Definition of zenith discrete angle.

is less than 2° for ZDAs greater than approximately 20°, reaching 6° at ZDAs of 10°. It must be noted that a similar result would be obtained by deriving $\delta\theta$ as a function of θ from Eq. (5). However, results are inaccurate at small θ, because the expression assumes only small changes in $\delta\theta$.

d. The VSP and its implication to clouds

The VSP can be used as a tool for measurements of radiation under cloudy conditions provided the cloud field is relatively static for any 2-min period. Should clouds move in or out of the line of the sun during any run, then application of the VSP sky distribution modeling presented here does not work, because of irregular fluctuations in irradiance.

In order to address this issue, it is necessary to have access to in situ information regarding the cloud movement for each particular run. This is achieved by observing the standard deviation (std dev) in signal output from another SLC instrument operating in tandem with the VSP-deployed instrument. By comparison of the visual form of many data runs with their corresponding

m^{-2} s^{-1}) and δD is the fraction of the total sky radiation D (in mW m^{-2}) that is measured by the sensor. To conserve units on both sides of the equation we need to divide δD by the increment of solid angle $\delta\Omega$ that is seen. Hence, the radiance value is estimated as the difference between consecutive sky-view irradiances divided by the incremental solid angle $\delta\Omega$.

To complete the sky-view analysis, it becomes necessary to integrate our derived radiance values across a finite ZDA interval (usually greater than 0.08 sr). This step becomes necessary due to the fine sky-area resolution between measurements at the bottom of the cylinder combined with the higher signal-to-noise ratios in the same cylinder region. The effect of this can be quantified by taking the derivative of both sides of Eq. (4) in order to derive an expression relating θ to Ω [Eq. (7)]. Here, θ_1 represents the change in angular portion of sky that will result for a ZDA of θ_2 and a finite steradian change $\Delta\Omega$ (where $\theta_1 < \theta_2$):

$$\theta_1 = \arccos\left[\frac{\Delta\Omega + 2\pi\cos(\theta_2)}{2\pi}\right]. \qquad (7)$$

Results show that for an incremental change in Ω of 0.1 sr (used in this study), the discrete angle resolution

TABLE 1. Selected clear-sky days (Hobart, Australia).

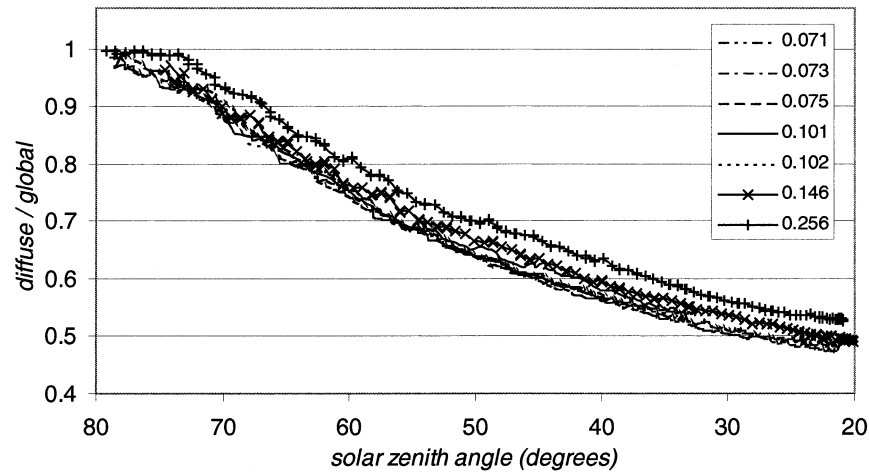| Date	Ozone column (DU)	Aerosol optical depth (308 nm)
14 Dec 1999	298	0.146
11 Jan 2000	286	0.256
12 Jan 2000	279	0.071
13 Jan 2000	276	0.101
24 Feb 2000	250	0.073
4 Mar 2000	282	0.235
20 Oct 2000	361	0.075
18 Nov 2000	337	0.102
20 Dec 2000	276	0.106
1 Feb 2001	278	0.135
3 Mar 2001	279	0.178

FIG. 6. VSP diffuse vs global UV-B ratio (with corresponding aerosol optical depth).

std dev's, it was found that the cloud field was relatively static if the std dev was less than 2.0 mW m^{-2} at low to moderate SZAs, and 1.0 mW m^{-2} or less at high SZAs, because of the reduced total signal for these conditions.

Once the "pseudo" static-cloud VSP dataset has been determined, the same VSP modeling as for clear-sky conditions can be applied to the "accepted" runs. As an extra modification here, for all SZAs less than 70°, if the direct beam was less than 2.0 mW m^{-2} then we assumed that the direct component was zero, and we included this in the relevant ZSV portion of the cumulative diffuse curve. For SZAs greater than 70° we ignored the modification because of the low direct irradiance values that may exist in this range.

3. Results

Much of this section refers to several clear-sky days extracted from the library archive of VSP measurements (Table 1). Recording of sky conditions was undertaken by manual observations at the Geography building roof climate station and cross-checked with 3-hourly cloud observations from the Hobart Bureau of Meteorology. For each of the days, the morning aerosol optical depth at both 412 and 867 nm was also obtained. This was undertaken by Langley analysis of a site-mounted Multi-Filter Rotating Shadowband Radiometer (MFRSR) manufactured by Yankee Environmental Systems. The aerosol optical depth was then assumed to be a logarithmic function of wavelength such that optical depth $(\tau_a) = \beta\lambda^{-\alpha}$ (Iqbal 1983). Here, α and β are the Ångström parameters obtained from the two measured wavelengths, and the optical depth was extrapolated to 308 nm. At 308 nm, the spectral response of the VSP-deployed SLC instrument is equivalent to the average of the complete UV relative response curve of the same instrument, which is justification for its use in this study.

a. Clear-sky irradiance

Figure 6 presents the VSP-measured diffuse versus global irradiance for seven clear-sky mornings. Data are drawn from Table 1, and the aerosol optical depth at 308 nm is used to differentiate each curve. The variation in low-SZA endpoint between mornings is due to the variation in solar noon SZA. The two high aerosol mornings (corresponding to 286 and 298 DU of ozone) are characterized by higher than expected diffuse/global ratios. This implies that aerosol attenuation, particularly on the two offending days, is perhaps dominated by scattering. Interestingly, for each of the ratio curves presented here, the variability as defined by the variance of the ratios appears to be the same at all SZAs. However, defined as a percentage of the irradiance, the variability increases with SZA. It is deemed that the variability increase is perhaps an artifact of the reduction in signal magnitude at high SZAs and is larger than the variation associated with cosine or VSP extraction errors.

The effect of aerosol can be precisely illustrated by a comparison of the ratio of total diffuse to direct irradiance for days of similar atmospheric ozone levels (Fig. 7). Here, 6 days in Table 1 correspond to ozone values from 276 to 282 DU, and the corresponding aerosol optical depths are evenly spread from 0.071 to 0.235. The compilation of this dataset was not trivial, because of the high prevalence of clear-sky days characterized by low aerosol optical depths since the start of the VSP measurement campaign.

Results clearly show the increasing effect of atmospheric scattering for an increase in SZA and aerosol optical depth. What is important here is that the curves are a strong function of the single-scattering albedo. Thus, results here may not be applicable to different conditions of this parameter; however, they emphasise what can be done with this type of instrument.
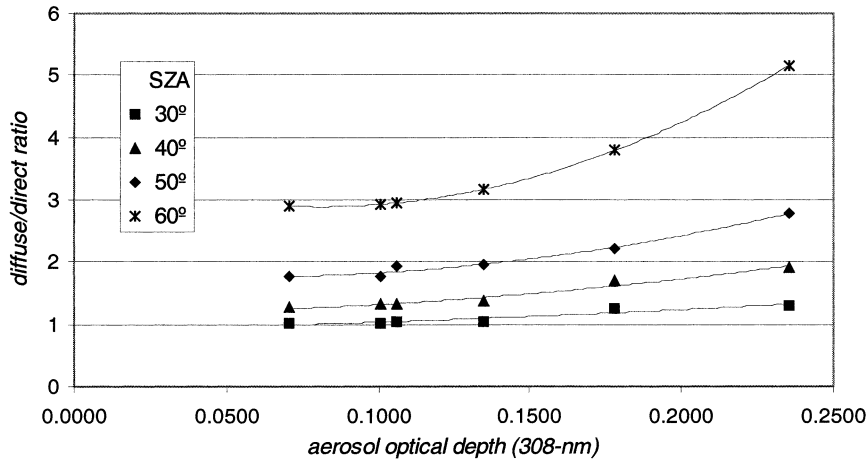
FIG. 7. Total diffuse/direct irradiance ratio vs aerosol optical depth at different SZAs; all measurements correspond to a total ozone column of 279 ± 3 DU.

b. Cloudy-sky irradiance

Figure 8 presents a time series of total diffuse irradiance superimposed on the global irradiance for the entire day on 6 December 2000. This day was characterized by 5 octas of cumulus cloud throughout most of the day. The mean SZA gap between consecutive VSP measurements is 0.98° because of the requirement of only accepting data that have a 2-min std dev in global UV-B irradiance less than 2.0 mW m^{-2}.

For the given cumulus cloud conditions, the importance of circumsolar radiation is emphasized. When the direct beam is unobstructed, a significant portion of the circumsolar component will reach the ground. Furthermore, it may also be enhanced by side reflection from clouds. Alternatively, when cloud cover blocks the direct beam, much of the circumsolar radiation is scattered back to space or scattered downward at a longer pathlength. These two extreme scenarios argue that if direct radiation increases (by virtue of not being blocked by a cloud), then so will the diffuse radiation and vice versa. This is particularly the case at low SZAs, as given by locations A and B in Fig. 8.

c. Sky radiance distribution

As the VSP measures an averaged radiance along a concentric ring portion of sky, it includes both circumsolar and background skylight components. The simple process of averaging smoothes the circumsolar signal. In the next section, all the VSP data presented will include both the radiance components mentioned.

1) CLEAR-SKY RADIANCE DISTRIBUTION

Figure 9 is another example of what can be done with the VSP. It gives some UV-B radiance distribution
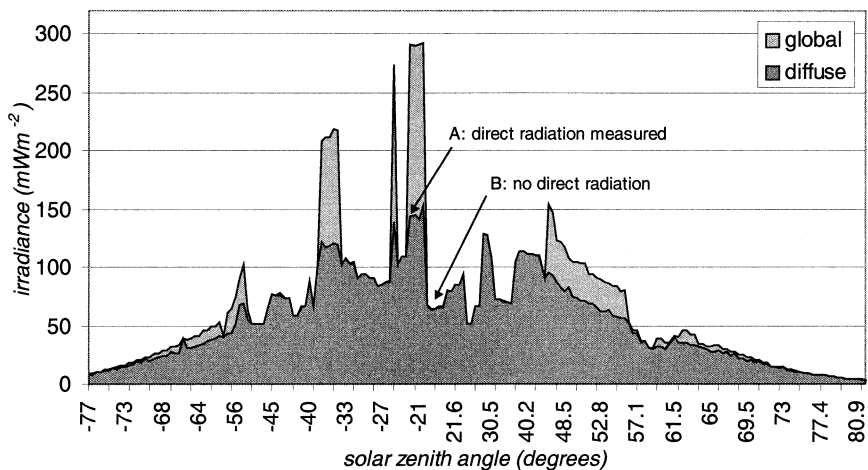

FIG. 8. VSP diffuse irradiance superimposed on global irradiance for a cloudy-sky day (6 Dec 2000, 5-octa cumulus).
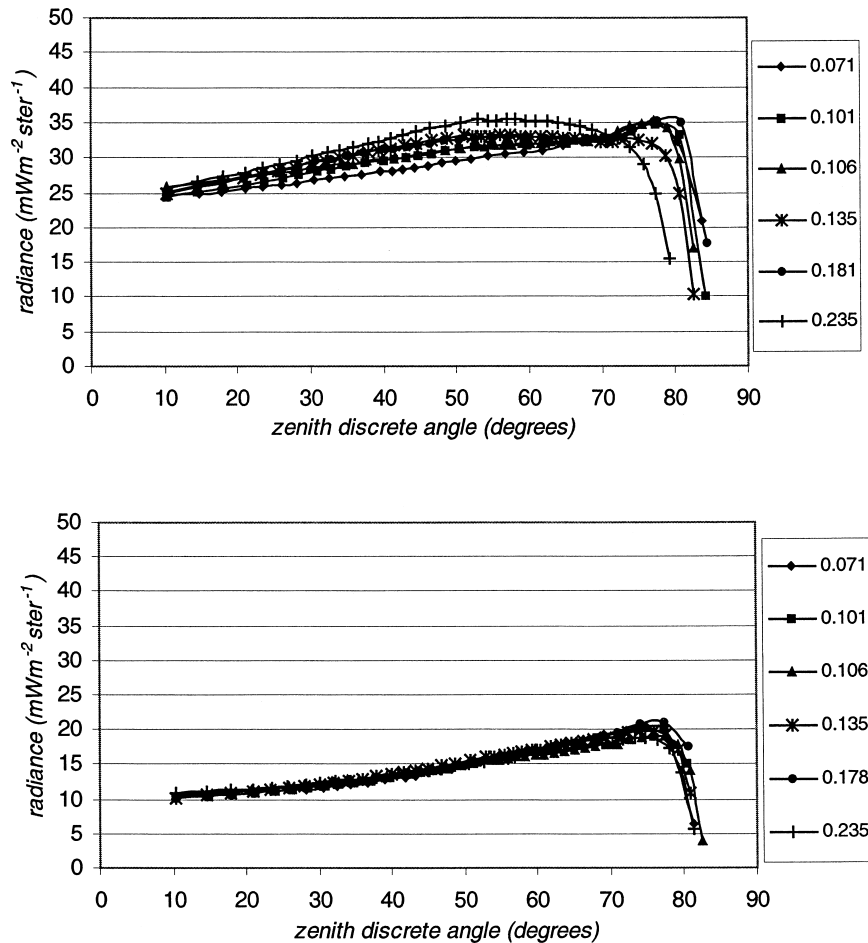
FIG. 9. VSP radiance distribution at (top) 40° and (bottom) 60° SZAs, with aerosol dependence.

curves (at SZAs 40° and 60°) parameterized according to the measured aerosol optical depth. Data were taken from the same VSP runs used for the total direct and diffuse values in Fig. 7 (at the given SZAs). As a reminder here, each curve corresponds to a different aerosol morning, and the daily total ozone column was almost the same across days. Sources of error include the assumption that atmospheric ozone and aerosol are constant throughout each morning.

In brief, the VSP results at 40° SZA indicate that the overall magnitude of each radiance curve increases with an increase in aerosol optical depth. This is to be expected because of the increase in scattering of the direct beam. In contrast, results corresponding to an SZA of 60° indicate that the effect of aerosols is small at low ZDAs. However, we notice some aerosol dependence near to the sun and at higher ZDAs.

Figure 9 also indicates a linear change in radiance distribution for all ZDAs less than approximately 70°. This is largely due to the trend reduction as a result of the azimuthal integration of the signal. In addition, for all ZDAs less than approximately 60°–70°, the slope of

each curve is positive, a trend experienced across many clear-sky days for which the VSP was operational. Based on these observations a model was developed in order to provide some explanation for this trend. Here, the average clear-sky radiance seen by the VSP may be written as

$$\overline{R} = (1 - L_1) \times R_{CS} + L_1 \times R_{SK}$$

$$\overline{R}' = (1 - L_1') \times R_{CS}' + L_1' \times R_{SK}'$$

$$L_1 = L_{SK}/(L_{CS} + L_{SK}); \qquad L_1' = L_{SK}'/(L_{CS}' + L_{SK}'), \quad (8)$$

where $\overline{R}$ is the mean radiance measured by the VSP, L_{CS} and L_{SK} are the mean lengths in the circumsolar (CS) and background skylight (SK) parts of the zenith, and R_{CS} and R_{SK} are the mean radiances in these two regions. Primes denote higher ZDAs, as in Fig. 10. Interestingly, UV-B radiance sky maps based on measurements by Blumthaler et al. (1996) and a combination of measurements and modeling by Grant et al. (1997a) indicate that the clear-sky UV-B radiance distribution is asymmetric in magnitude about the solar disk and possibly
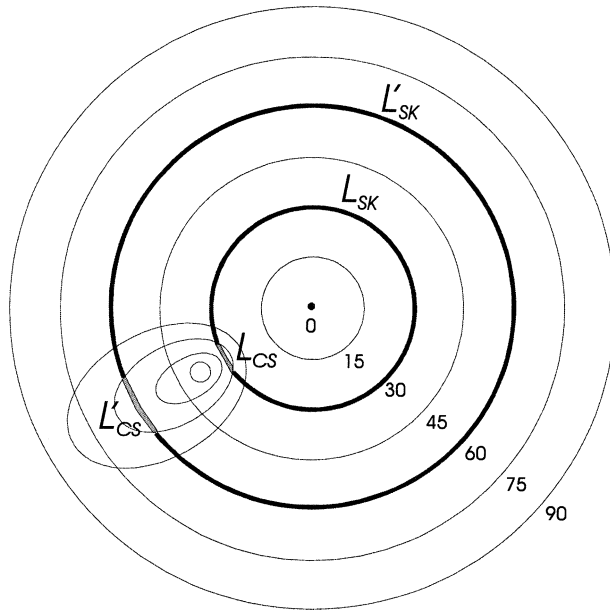
FIG. 10. Asymmetric circumsolar component about the sun; the circumsolar gradient is smaller at higher ZDAs.

resembles the form shown in Fig. 10. The only exception here is for isopleths perhaps very close to the sun where symmetry is radial. Hence, we can use Eq. (8) to relate observed VSP clear-sky radiance data with Fig. 10 as follows: First, assume $R_{CS} \gg R_{SK}$ and that R_{SK} is relatively constant with zenith angle; R_{SK} has in fact been shown to vary from a maximum toward the horizon to a minimum toward the zenith and as such resembles a saucer-shaped distribution (Ireland and Sacher 1996). Since L_1 increases with zenith angle, the only time $\overline{R}$ also increases with zenith angle is when $R'_{CS} \gg R_{CS}$. This may be the case for portions of each radiance curve with a positive slope in Fig. 9, but more analysis is required to support this claim.

2) CLOUDY-SKY RADIANCE DISTRIBUTION

Coombes and Harrison (1988) and Brunger and Hooper (1993) show that for thinly overcast skies it is possible to observe significant brightening near the solar position with a resultant azimuthal anisotropy. However, the circumsolar and background skylight components are generally much less defined than that for clear skies because of the increase scatter imparted by cloud (Grant et al. 1997b; Grant and Heisler 1997). In order to illustrate the performance of the azimuthally averaging VSP under cloudy conditions, each ZDA average radiance value $\overline{R}_\theta$ is first normalized to the total diffuse irradiance D for each VSP run such that

$$f(\theta) = \frac{\overline{R}_\theta}{D}. \qquad (9)$$

Here, $f(\theta)$ is proportional to $\overline{R}_\theta$ in any direction, and

the implication is that the difference across any zenith curve is now largely due to cloud distribution.

Figures 11a and 11b present some 2-min UV-B radiance distribution curves from the 6 December (5-octa cumulus) and 21 December 2000 (6-octa stratocumulus), respectively. In both graphs, each VSP run represents a different morning or afternoon SZA. Figures 12a and 12b present some alternate VSP radiance curves for varying levels of cumulus and stratocumulus cloud cover, respectively. Here, an attempt was made to select VSP runs corresponding to the same SZA (Table 2). The VSP radiance integration resolution of 0.1 sr is the same as that utilized throughout the study, and hence the discrete angular resolution is quite fine.

All graphs provide some indication as to the positional thickness of the given cloud type. However, it cannot be assumed that the data relate to the sky position of cloud alone. This is clarified by measurements of sky radiance undertaken during broken cloud conditions by Weihs et al. (2000) where the cloud radiance measured at the observer was shown to be dependent upon the scattering angle as well as cloud properties.

Although data are limited, a comparison of results presented in Figs. 11 and 12 indicates several features. First, the overall trend for each of the VSP runs appears to be less dependent on scattering angle for conditions of stratocumulus cloud. For cumulus conditions, a variation in scattering angle (by way of variation in SZA) may lead to markedly different overall trends, which can be explained by the variation in cloud side reflection that is possible due to the greater vertical extent of cumuliform clouds.

Second, the radiance variation as a function of ZDA appears to be similar for different conditions of medium to high cloud cover. That is, the period of the high-frequency oscillation in each of the graphs is similar. This may be an artifact of the spatial distribution of the particular cloud and is worthy of further exploration. For low cloud cover (2 octas), the radiance profile tends to approach the clear-sky scenario and is likely to be a result of cloud positioned away from the sun–sensor path. In this situation, the sensitivity of the sensor may be a limiting factor.

Third, the stratocumulus graphs display a near-horizontal trend for ZDAs less than 50°–60°. This indicates that at low to moderate ZDAs cloud reflection may be Lambertian in character. It also implies that the clouds may be relatively thick in nature. The asymmetry factor of stratocumulus clouds approximates +0.8 to +0.9, with slight dependence on droplet radius (Hu and Stamnes 1993). A relatively thin stratocumulus layer would perhaps show radiances more biased toward the directional component of this asymmetry. At high ZDAs and moderate to high cloud cover we see a downward trend in Figs. 11b and 12b. This is because for high ZDAs with clouds near the horizon, the pathlength to the sensor is so large that the extinction (scattering and ab-
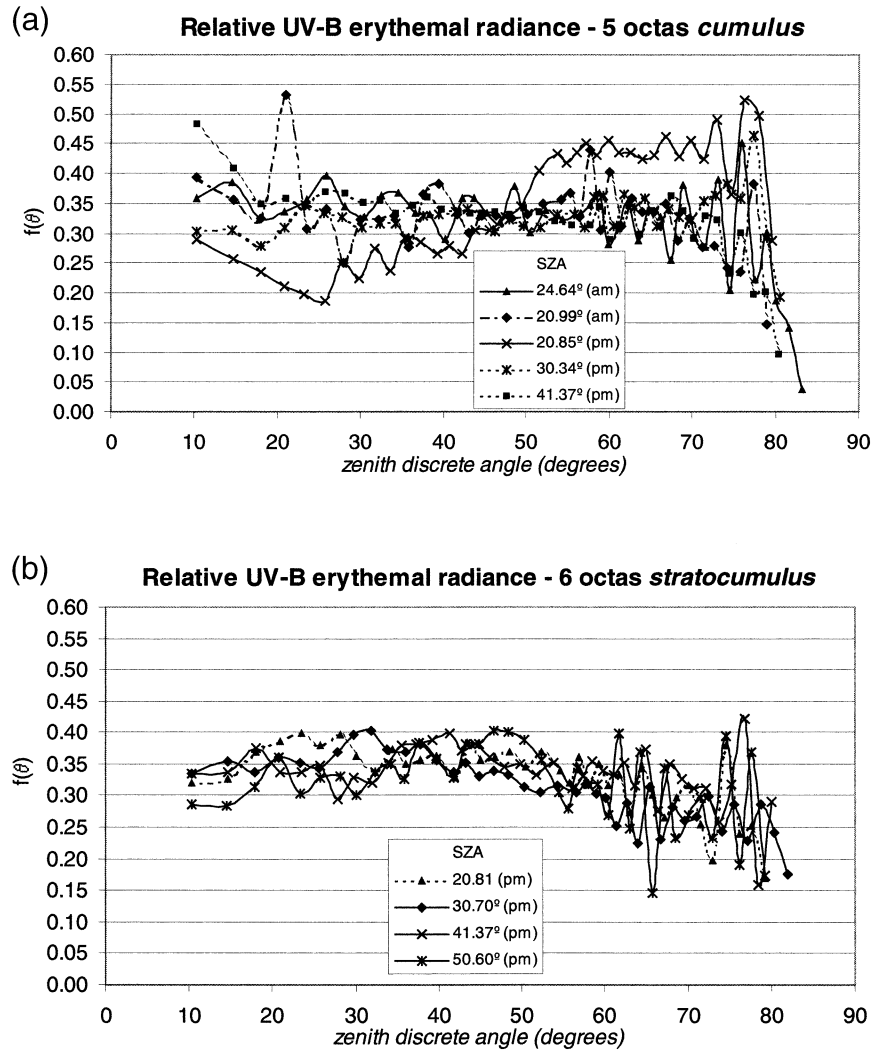
(a)

(b)

FIG. 11. Relative radiance distribution: (a) 5-octa cumulus cloud and (b) 6-octa stratocumulus cloud.

sorption) is also large. Overall, the brief results highlight what can be explored with the VSP given more data.

4. Summary and conclusions

Particular care was taken in this study to ensure accuracy and precision in the two most essential features of the VSP: the accurate separation of direct and diffuse irradiance and further separation of the resultant diffuse component into azimuthally averaged radiances at different zenith angles. Integration of cosine-corrected radiances then provides a global diffuse measurement corrected for an anisotropic sky. Future hardware changes include variable speed sensor movement for improved data sampling and cylinder internal baffles for reduced internal reflection. Both are intended to improve data quality.

The radiance azimuthal dependence cannot be separated using the VSP alone; however, this does not detract from

TABLE 2. Various VSP runs for Figs. 12a and 12b cloud cover analyses.

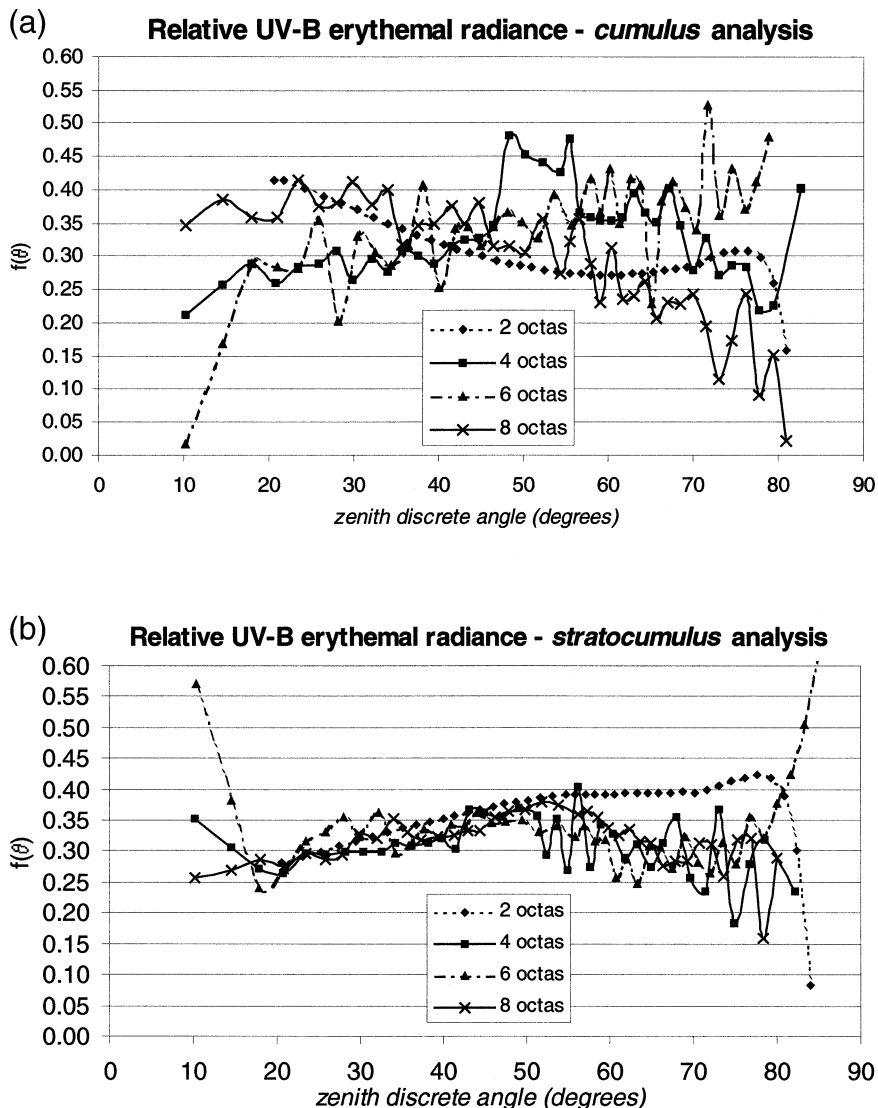| Cloud cover (octas)	Fig. 12a (cumulus)		Fig. 12b (stratocumulus)	
	Date	SZA	Date	SZA
2	19 Sep 2000	48.59 (P.M.)	15 Nov 2000	42.62 (A.M.)
4	6 Dec 2000	49.12 (P.M.)	12 Dec 2000	42.53 (P.M.)
6	29 Dec 2000	49.15 (P.M.)	12 Dec 2000	41.07 (A.M.)
8	22 Dec 2000	48.32 (A.M.)	21 Dec 2000	41.37 (P.M.)

FIG. 12. Relative radiance distribution: (a) cumulus analysis and (b) stratocumulus analysis.

the usefulness of the system. VSP results on cloudy days indicate a fine structure in the sky radiance variability as a function of ZDA. In some instances, changes are significant across ZDAs of 2°–3°, equivalent to the angular resolution of the VSP. A recently deployed sky digital camera will improve the scheme further by providing images that indicate cloud azimuthal information. Radiometric azimuthal information can also be added by periodic operation of a fast sky-tracking spectroradiometer.

Instrument sensitivity is an added concern with regards to VSP erythemal radiance measurements as a function of aerosol. Introduction of a longer-wavelength broadband instrument would perhaps divulge greater aerosol sensitivity, because aerosol scattering would be less masked by the Rayleigh scattering component. Incorporation of a narrowband mulitfilter instrument would further introduce spectral information to the

scheme. If selected wavelengths are similar to MFRSR channels (refer to Michalsky et al. 1987), then VSP direct-beam extraction would allow for Langley analysis of data. A particular feature of MFRSR entrance optics is their relatively small size. If deployed in the VSP, direct-beam retrieval of spectral irradiance would perhaps be more precise. This is because the transition from diffuse to global radiation for an upward-moving instrument would be almost instantaneous, thus avoiding any transition zone extrapolation uncertainty. This in turn would allow for exact representation of near-sun circumsolar irradiance at all SZAs. It is important to remember that an alternate to the SLC erythemal instrument must have good time-response characteristics. In addition, the cosine error must be known to a high degree of accuracy.

In conclusion, the sky-tracking speed of the VSP is

much faster than most other tracking instruments currently available. In addition, the total cost of the VSP prototype utilized in this study is significantly less than most sky-scanning instruments (approximately $5000, not including sensor and calibration costs). With some minor modifications it is deemed that the VSP has many applications for long-term spatial and temporal radiometric measurement of radiation, both at the UV and visible regions of the solar spectrum.

REFERENCES

Beaglehole, D., and G. G. Carter, 1992: Antarctic skies, 2. Characterization of intensity and polarization of skylight in a high-albedo environment. *J. Geophys. Res.,* **97,** 2597–2600.

Blumthaler, M., J. Gröbner, M. Huber, and W. Ambach, 1996: Measuring spectral and spatial variations of UVA and UVB sky radiance. *Geophys. Res. Lett.,* **23,** 547–550.

Brunger, A. P., and F. C. Hooper, 1993: Anisotropic sky radiance model based on narrow field of view measurements of shortwave radiance. *Sol. Energy,* **51,** 53–64.

Coombes, C. A., and A. W. Harrison, 1988: Angular distribution of overcast sky short wavelength radiance. *Sol. Energy,* **40,** 161–166.

Dichter, K., 1993: Fluorescent-phosphor-based broadband UV light sensors. *Sensors,* Helmers Publishing, Inc., 19, 21–24.

Grant, R. H., and G. M. Heisler, 1997: Obscured overcast sky radiance distributions for ultraviolet and photosynthetically active radiation. *J. Appl. Meteor.,* **36,** 1336–1345.

——, ——, and W. Gao, 1997a: Clear sky radiance distributions in ultraviolet wavelength bands. *Theor. Appl. Climatol.,* **56,** 123–135.

——, ——, and ——, 1997b: Ultraviolet sky radiance distributions of translucent overcast skies. *Theor. Appl. Climatol.,* **58,** 129–139.

Hu, Y. X., and K. Stamnes, 1993: An accurate parameterization of the radiative properties of water clouds suitable for use in climate models. *J. Climate,* **6,** 728–742.

Iqbal, M., 1983: *An Introduction to Solar Radiation.* Academic Press, 390 pp.

Ireland, W., and R. Sacher, 1996: The angular distribution of solar ultraviolet, visible and near-infrared radiation from cloudless skies. *Photochem. Photobiol.,* **63,** 483–486.

Kuchinke, C., and M. Nunez, 2001: Spectral dependence in the cosine response of broadband UV instruments. *J. Geophys. Res.,* **106** (D13), 14 287–14 300.

Michalsky, J. J., L. C. Harrison, and B. A. Lebaron, 1987: Empirical radiometric correction of a silicon photodiode rotating shadowband radiometer. *Sol. Energy,* **39,** 87–96.

Morys, M., and D. Berger, 1993: The accurate measurement of biologically effective ultraviolet radiation. *Atmospheric Radiation,* K. H. Stamnes, Ed., SPIE Proceedings, Vol. 2049, SPIE, 152–161.

Nield, K. M., A. Bittar, and J. D. Hamlin, 1997: Development of an all-sky scanning spectroradiometer with a visible diode array and a near-infrared acousto-optic tunable filter. *Appl. Opt.,* **36,** 7939–7947.

Panofsky, H. A., and G. W. Brier, 1968: *Some Applications of Statistics to Meteorology.* The Pennsylvania State University, 224 pp.

Robertson, D. F., 1972: Solar ultraviolet radiation in relation to human sunburn and skin cancer. Ph.D. thesis, University of Queensland, St. Lucia, Australia, 179 pp.

Weihs, P., A. R. Webb, S. J. Hutchison, and G. W. Middleton, 2000: Measurements of the diffuse UV sky radiance during broken cloud conditions. *J. Geophys. Res.,* **105** (D4), 4937–4944.